metals

Article

Microstructure and Mechanical Behaviors of Fiber-Laser-Welded QP980-QP1180 Steels

Hafize Çelik [1,2,*] and Onur Saray [1]

[1] Department of Mechanical Engineering, Bursa Technical University, 16310 Bursa, Turkey; onur.saray@btu.edu.tr
[2] TOFAS R&D Center, Turkish Automobile Factory, 16110 Bursa, Turkey
* Correspondence: hafize.celik@tofas.com.tr or 162080202@ogr.btu.edu.tr; Tel.: +90-549-694-8187

Abstract: Advanced high-strength steels are considered the first choice when manufacturing lighter vehicles. Quench-partitioning (QP) steels are good candidates that fulfill manufacturing and performance requirements with their outstanding strength and formability. Laser welding offers a productive solution to the challenges of liquid metal embrittlement due to a low heat input and higher welding efficiency. This study investigated the microstructural evolution and mechanical performance of dissimilar laser-welded joints between QP980 and QP1180 steels. The microstructure of the joint mainly consisted of martensite phase in the fusion zone (FZ) and super-critical heat-affected zone (HAZ). In the mid and sub-critical HAZ, the microstructure consisted of tempered martensite along with ferrite and retained austenite on both sides. Due to these microstructural evolutions, FZ and HAZ are strengthened, and thus, laser welds can be achieved without the formation of a visible soft zone. Fracture of the joints occurred in softer base metal (BM) with ductile characteristics without any considerable strength loss. However, the ductility of the joints was lower than that of BMs because of deformation localization due to microstructure, yield strength, and thickness variations in the tensile and Erichsen test specimens. These results show that laser welding can be considered an effective alternative for joining QP steels.

Keywords: advanced high-strength steels (AHSSs); quench-partitioning (QP) steels; scanning electron microscopy (SEM); electron backscatter diffraction (EBSD); fiber laser welding; Erichsen; mechanical testing

check for updates

Academic Editor: Andrea Di Schino

Received: 16 January 2025
Revised: 4 February 2025
Accepted: 7 February 2025
Published: 9 February 2025

Citation: Çelik, H.; Saray, O. Microstructure and Mechanical Behaviors of Fiber-Laser-Welded QP980-QP1180 Steels. *Metals* **2025**, *15*, 174. https://doi.org/10.3390/met15020174

Copyright: © 2025 by the authors. Licensee MDPI, Basel, Switzerland. This article is an open access article distributed under the terms and conditions of the Creative Commons Attribution (CC BY) license (https://creativecommons.org/licenses/by/4.0/).

1. Introduction

The European Union Green Deal in the automotive industry aims to reduce carbon emissions to 55% of the levels of 1990 (Fit 55) and to make European nations carbon neutral by 2050 [1]. Today, compliance with the Green Deal is among the priority research and development (R&D) targets and innovation issues. Compliance with the Green Deal is a hard task that requires optimizing design and manufacturing processes to reduce carbon dioxide emissions [2]. Some automotive companies have committed to achieving carbon net zero targets earlier than 2050 [3]. Since vehicle weights and carbon emission production are directly related, conducting R&D studies on designing and manufacturing lighter vehicles has been one of the important targets of automotive manufacturers in recent years. For this reason, new-generation high-strength steel sheets that provide a good balance of formability and strength have been used widely [4]. Recently, higher strength levels with an acceptable level of formability have been achieved by developing third-generation AHSSs [5]. Although this generation is still under development, numerous members

like QP steels, medium manganese steels, and transformation-induced plasticity (TRIP)-aided bainitic ferritic (TBF) steels have attracted considerable attention. However, QP steels have shown the most advanced development among other third-generation AHSS members [6] and have attracted more attention in the automotive industry. QP steel is produced on a specialized line designed to heat steel sheets to austenitize and then cool rapidly to an intermediate temperature between Ms and Mf to achieve a microstructure made up of martensite (M) and austenite after cold rolling. The sheet is then reheated to a temperature above Ms for partitioning, enabling carbon (C) to migrate from the M into the untransformed austenite. The increased carbon content helps to stabilize the austenite after it cools to room temperature [7]. Consequently, a final microstructure may develop that includes M along with either retained austenite (RA) or a combination of ferrite (F), M, and RA. In this microstructure, the initial M phase contributes to the high strength of the steel, while the TRIP effect of the RA phase enhances both the strength and formability of the steel, aided by improved strain hardenability [7]. Because of the exceptional toughness and improved plasticity provided by the QP mechanism, QP steels are among the most advanced steel grades developed to be used in the manufacturing of crash energy absorption parts like crash beams, inner door crash beams, and A-B pillars of vehicles [8,9].

It is also known that such a good balance of the strength and formability of the high strength automotive steels is metastable [10]. Especially, thermal processes like welding as the major joining technique used in Body in White (BIW) are extremely effective on the well-engineered microstructures and mechanical properties of the AHSSs. Considering that AHSSs are indispensable for manufacturing structural parts of vehicles, their share is expected to increase in the near future [10]. This expectation inevitably requires the process parameters and performance interactions to be examined and known to successfully design and manufacture parts from these new-generation high-strength sheets [11].

According to conventional welding methods, laser welding has become widespread in automobile production day by day. This is mainly due to the highly concentrated beam of energy being directly exposed to the joining region; for example, the area under heat exposure is smaller in laser welding compared to conventional joining methods like spot welding or arc welding [12]. Moreover, the energy efficiency of laser welding is higher, the process cycle time is shorter, and it is more suitable for automation [13,14]. Wang et al. showed that laser welding QP1180 steel resulted in superior properties such as a narrower HAZ and higher strength compared to those of the gas-metal-arc-welded and friction-stir-welded counterparts [15]. Since laser welding performance depends on many parameters, it is very important to determine how the laser welding parameters affect the final product performance. Although the laser type, laser power, and laser speed are among the parameters responsible for overall weld seam performance, extensive research efforts have revealed that the pulse duration, pulse frequency, overlap, laser beam diameter, focal distance, and heat input are other important parameters that should be selected wisely for excellence in laser weld seam [16–18].

The laser welding of similar QP steels has been the subject of recent studies. Xue et al. laser welded 1.22 mm thick QP980 sheets using a welding energy of around 60 J/mm and investigated the HAZ microstructure and the tensile behavior. Comprehensive microstructural examinations indicated that granular carbides are precipitated at the boundaries of the M blocks at the sub-critical HAZ region, which lead to lower strength and higher ductility compared to those of the BM and FZ [19]. Guo et al. studied the strain rate-dependent mechanical properties and fatigue performance of laser-welded 1.36 mm thick QP980 steel joints. The joining process was performed at a weld energy of about 34 J/mm. The positive strain rate dependency of the joint strength with a decline in ductility was observed. The

fatigue strength of the joint, on the other hand, was determined to be lower than that of the BM [20]. Zhang et al. studied the effect of water cooling assistance to improve the mechanical properties and fatigue resistance of QP980 steels laser welded with a welding energy of about 80 J/mm. The results indicate that cooling assistance resulted in a decrease in weld softening and caused an improvement in both the joint strength and fatigue crack growth behavior [21]. In addition, Zhang et al. proposed the cooling-assisted welding method to decrease heat input during welding, which decreases the softening and grain size of FZs. The water cooling assistance method is proposed to be applied during the laser welding of QP980 steel to improve the softening and fatigue performance of welded joints. The width of the softening zone in water cooling assistance-welded joints was found to be narrower, and the fatigue life was found to be improved compared to that of traditional welded joints [21]. Zahrani et al. showed in their study that with an increase in the welding heat input, the fusion zone hardness was essentially unaffected. However, owing to an increase in the tempering time during laser welding, the softened zone experienced an intense hardness drop, and its width became broader (∼0.6–1.6 mm) at higher heat inputs. The yield and ultimate tensile strength of the joints decreased by increasing the heat input [22]. Fang et al. (2014) proposed the regeneration treatment to avoid the degradation of the mechanical properties of the welded structures. This technique involves transferring the as-welded joint into a furnace and holding it at a suitable temperature for a sufficient duration to transform the austenite, formed by the heat input of the welding process, into bainite, thereby preventing its transformation into brittle martensite during cooling to room temperature. This combination of the welding procedure and heat treatment results in weldments not affected by cold cracks or martensite in the weld zone and the general degradation of the mechanical properties [23]. The industrial application of dissimilar laser welding methods for first- and third-generation AHSS has been the subject of previous studies and resulted in an acceptable level of joint strength, leading to several design opportunities and enhancing the mechanical performance of the BIW parts [24–26]. In a limited number of studies, laser-welded joint formability has been studied as an important mechanical behavior determining the compatibility to manufacturing schemes in the automotive industry. However, the laser-welded joints of TRIP800-QP980 steels [27] and QP980 and martensitic steels exhibited limited formability compared to BMs [28,29].

Due to the well-engineered microstructure and the balance of strength and ductility, laser-welded QP steels may provide a good opportunity to manufacture high-strength tailor-welded blanks to be used in forming high-performance body parts. However, it is understood from the current state of the art that the formability of laser-welded high-strength QP steels has been the subject of a limited number of studies. From this point of view, the aim of the current study was to investigate the microstructures, mechanical properties, and formability of laser-welded joints between QP980 and QP1180 steel sheets to reveal the potential of QP steels in the manufacturing of high-strength and lightweight BIW part manufacturing. From this point of view, the motivation of the current study is mainly to fill the gap in the literature on the formability of high-strength QP steels.

2. Materials and Methods

2.1. Materials and Laser Welding Process

In this study, 3rd-generation 1.2 mm thick uncoated QP980 and 1.5 mm thick hot-dip galvanized QP1180 AHSS steel was used and welded with fiber laser as butt joint configuration to consider material, thickness, and coating dissimilarity, as shown in Table 1. The QP steels were supplied by Baosteel Company (Baoshan Iron & Steel Co., Ltd., Shanghai, China).

Table 1. Steels used in this study.

Steel Grade	Coating	Thickness
QP980	Uncoated	1.2 mm
QP1180	GI (hot-dip galvanized coating)	1.5 mm

The sheet plates were cut into 155 mm × 490 mm sample sizes and prepared with laser cutting to avoid geometrical errors and/or contact errors in the mating surfaces. Samples were placed on laser machine rollers in a rolling direction that coincided with the joining direction, as shown in Figure 1. The maximum output power of the laser welding unit in continuous operating mode was 25 kW. In each welding process, the axis distances of the laser head were adjusted from the PLC control unit so that the head moved smoothly along the contact surfaces of the sheet materials to be welded. Dissimilar materials were welded under an argon (Ar) atmosphere with a shielding gas flow rate of 10 L/min using a welding power and a feed rate of 6 kW and 5 m/min., respectively, from the point (red), as shown in Figure 1d.

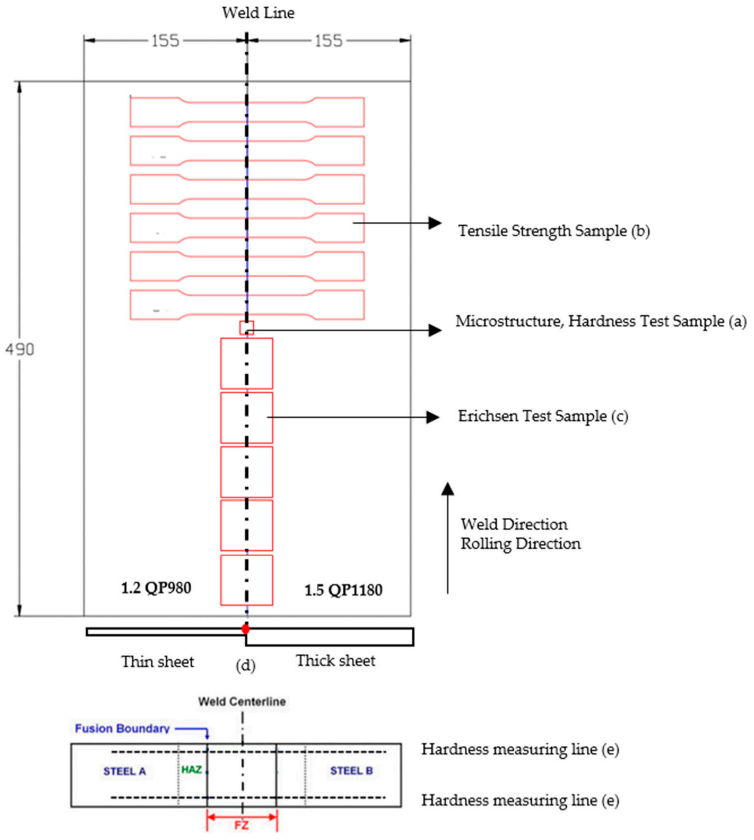


Figure 1. Schematical representation of locations of samples subtracted from laser-welded joints: (**a**) microstructure and hardness specimen; (**b**) tensile test specimen; (**c**) Erichsen cupping test sample; (**d**) point (red) where sheets are joined; (**e**) lines where microhardness measurement is taken from laser-welded sheets and laser welding thermomechanical regions.

Microstructural and mechanical characterization samples were extracted from the middle of the weld line after laser welding, as shown in Figure 1. Samples were cut with the wire electrical discharge machining (EDM) technique to avoid the effects of heat input.

2.2. Microstructural Characterizations

Samples were prepared for SEM following standard grinding, polishing, and etching, as well as for EBSD (with EDAX (EDAX Inc., Mahwah, NJ, USA) Hikari Pro detector). For

EBSD analysis, samples were polished with 0.05 µm colloidal silica for final polishing and then cleaned in an ultrasonic cleaner for 10 min. EBSD examinations were performed using the EDAX/TSL EBSD system connected to a Zeiss Merlin FEG-SEM (Zeiss, Oberkochen, Germany) scanning electron microscope and a EDAX Hikari EBSD camera (EDAX Inc., Mahwah, NJ, USA). Since the interaction depth of the EBSD technique varies between 5 and 10 nm, the sample surfaces were prepared to be completely free of errors. Data were collected in the area of 52 × 106 μm^2 for each thermomechanical region. Samples for microstructural characterization were extracted from the weld line, as shown in Figure 1a, and EBSD tests were conducted at 19 °C.

2.3. Mechanical Characterizations

Microhardness of the joining regions was determined by Vickers hardness measurements taken on the cross-section of the weld seam to reveal strength variations in welding process-induced thermomechanical regions, namely fusion zone (FZ), heat-affected zone (HAZ), and base metal (BM), as shown on Figure 1e. Microhardness measurements were performed with an indentation load of 200 g and a dwell time of 10 s on mirror-polished samples. Microhardness measurements were made on a Zwick/Roell ZHV 10 (Zwick-Roell, Ulm, Germany) brand Vickers microhardness measuring device. All measurements were carried out according to EN ISO 6507-1:2018 standard. Measurements were made in a linear line on the BM, HAZ, and FZ, and again on the BM at symmetrical and regular intervals. By creating a matrix with points separated by 0.10 mm, a total of 20 points was measured, and sample hardness values were determined as shown in Figure 1e.

Samples for tensile tests were extracted from the weld line, as shown in Figure 1b, and tests were performed at room temperature. Tensile test samples were cut in accordance with the EN ISO 6892-1:2009 (2019) standard, with the weld metal at the center of the sample. Samples were tensile tested at a strain rate of approximately 0.5 mm/s, tested on a Zwick Z300 (Zwick-Roell, Ulm, Germany) type uniaxial tensile testing machine (load cell capacity 300 kN). To understand the repeatability, the average values and standard deviation of at least 6 test results were calculated. Each sample was carefully connected to the tensile test device, and since there was a difference in thickness in the welded samples, care was taken to make connections in a way that would not cause the samples to bend.

Erichsen cupping test was performed to determine the formability of laser-welded steels. Samples for the Erichsen cupping test were extracted from the weld line, as shown in Figure 1c, in dimensions of 100 mm × 100 mm according to ISO 20482:2013 and tested at room temperature. Erichsen tests were performed at a spherical punch speed of 10 mm/min cut into specimens. At least five tests were performed to ensure repeatability of the results.

3. Results and Discussion

3.1. Metallographic Characterization

3.1.1. Microstructure of BMs

EBSD maps showing the distribution of Face-Centered Cubic (FCC) and Body-Centered Cubic (BCC) structured phases, crystallographic orientation distribution, and grain boundary characteristics of QP980 base metal are given in Figure 2. From the figure, it is understood that the microstructure of QP980 steel consists of RA, F, and M phases. Iron (Gamma) in Figure 2b shows the RA volume fraction. As can be understood from Figure 2b, the volume fraction of the RA is determined as 8.4% in the microstructure of QP980 steel. When the orientation map given in Figure 2b is examined, fine M phase particles are seen to be distributed in the ferritic matrix with a grain size of about 5 µm. The M phase seems to be nucleated at F grain boundaries. The volume fraction of the high angle grain boundaries (HAGBs) was measured at 88% in the as-received microstructure of the

QP980 steel (Figure 2c). Due to the existence of well-separated fine M grains, the average grain size diameter of the structure was determined as 0.57 μm (Figure 3). The grain size in both samples varied between 0.32 μm and 6.94 μm. The grain size distribution map also indicates the existence of ultra-fine grains with a grain size below 1 μm and a volume fraction of about 23%.

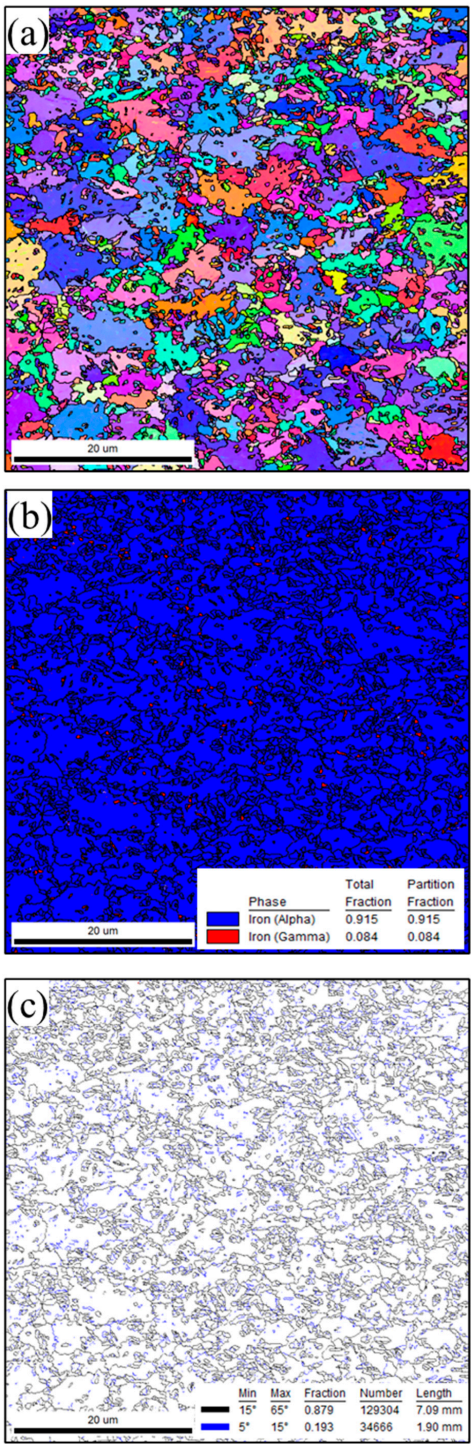


Figure 2. EBSD maps of QP980 BM: (**a**) crystallographic orientation distribution map; (**b**) distribution of FCC and BCC structured phases; (**c**) grain boundary distribution map.

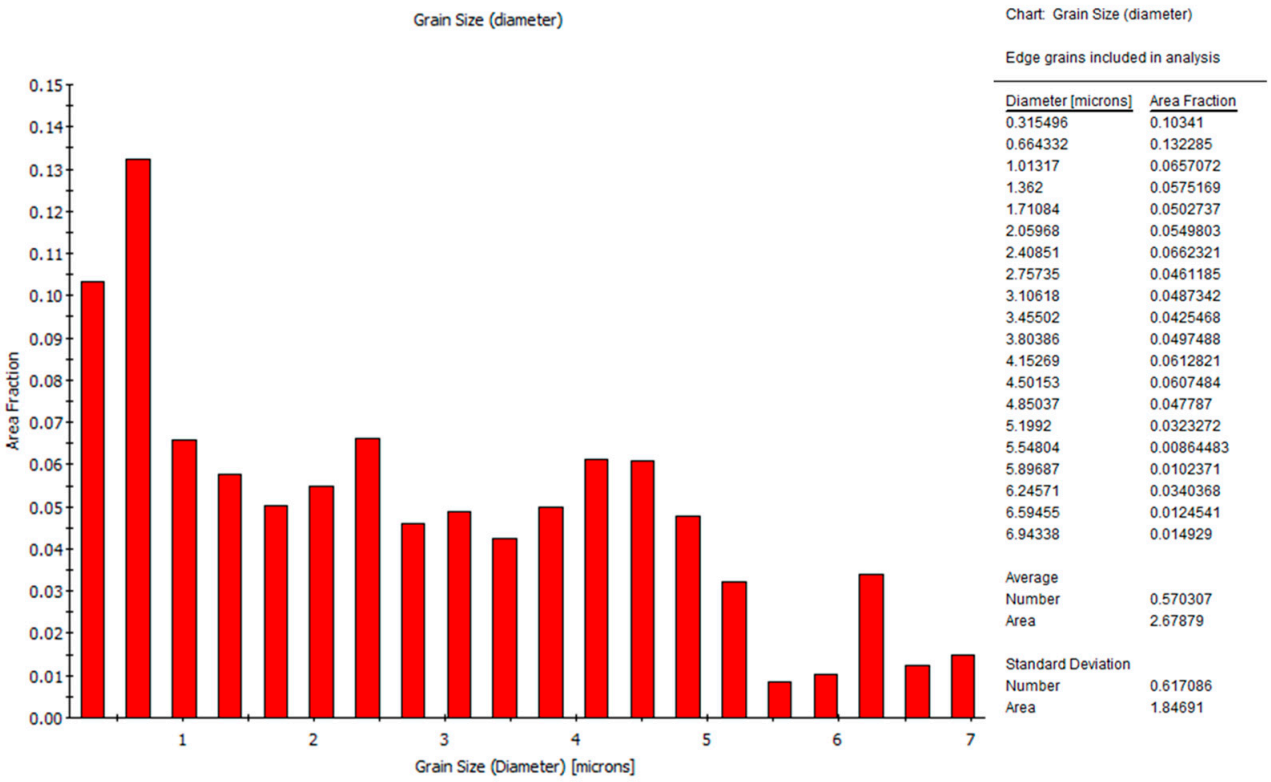


Figure 3. QP980 base metal grain size distribution histogram.

EBSD maps of QP1180 steel showing the distribution of FCC and BCC structured phases, crystallographic orientation distribution, and grain boundary characteristics are presented in Figure 4. The microstructure of the QP1180 steel mainly consisted of similar phases, including M, RA, and F, to those of the QP980 steel. However, the microstructural features of the QP1180 steel differed from those of the QP980 steel through the volume fraction and morphological features of the M phase. Iron (Gamma) in Figure 4b shows the RA volume fraction. As can be understood from the figure, the volume fraction of the RA is determined as 8.4% in the microstructure of the QP1180 steel. This value is quite similar to that of the QP980 steel (Figure 4a). However, M phase grains partly transformed into coarser grains more than well-separated particles. Also, the F grain size seems finer in the microstructure of the QP1180 steel, with a range of about 2–3 μm (Figure 4b). The volume fraction of the HAGB was measured at 74% in the as-received microstructure of the QP1180 steel (Figure 4c). Compared to QP980 steel, the lower value of the HAGB fraction may be related to the sub-grain boundaries of the martensite phase due to the lath-like morphology because boundaries separating crystals with misorientation angles lower than 15 ° mainly concentrated in the martensite boundaries as the strait lines through the grains (Figure 4c). Due to the existence of well-separated fine M grains, the average grain size diameter was 0.66 μm. The grain size at both samples varied between 0.27 μm and 5.47 μm. The grain size distribution map also indicates that the existence of ultra-fine grains with a grain size below 1 μm and a volume fraction of about 29% also supports this idea (Figure 5).

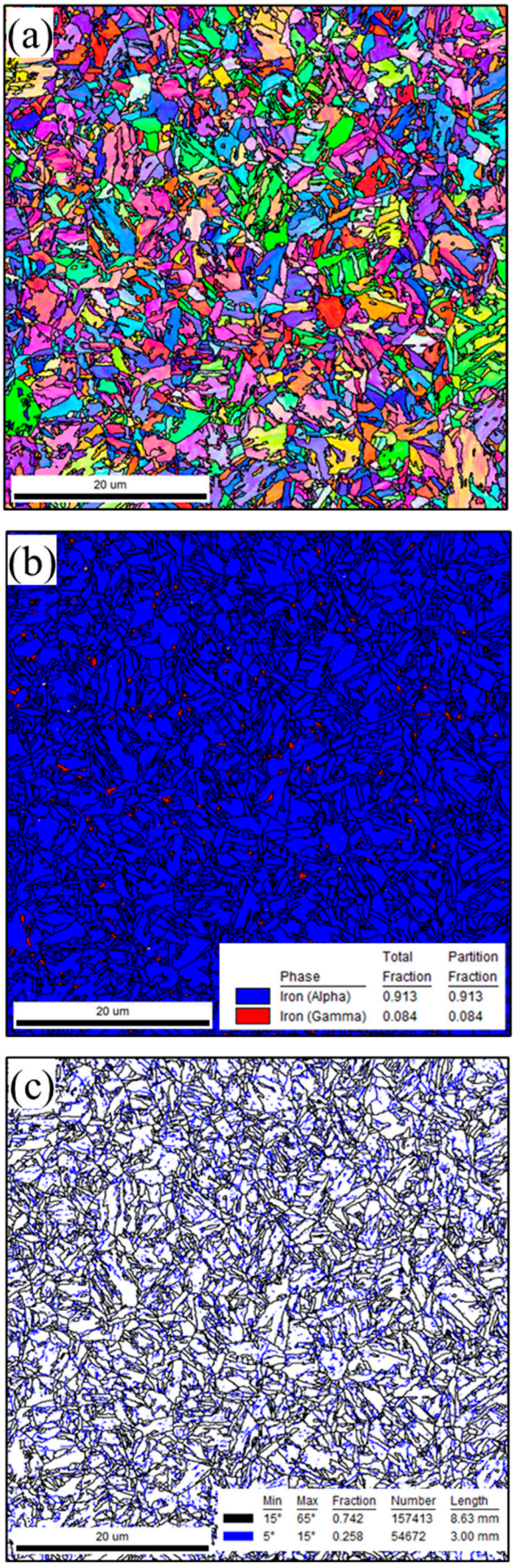


Figure 4. EBSD maps of QP1180 base metal: (**a**) crystallographic orientation distribution map; (**b**) distribution of FCC and BCC structured phases; (**c**) grain boundary distribution map.

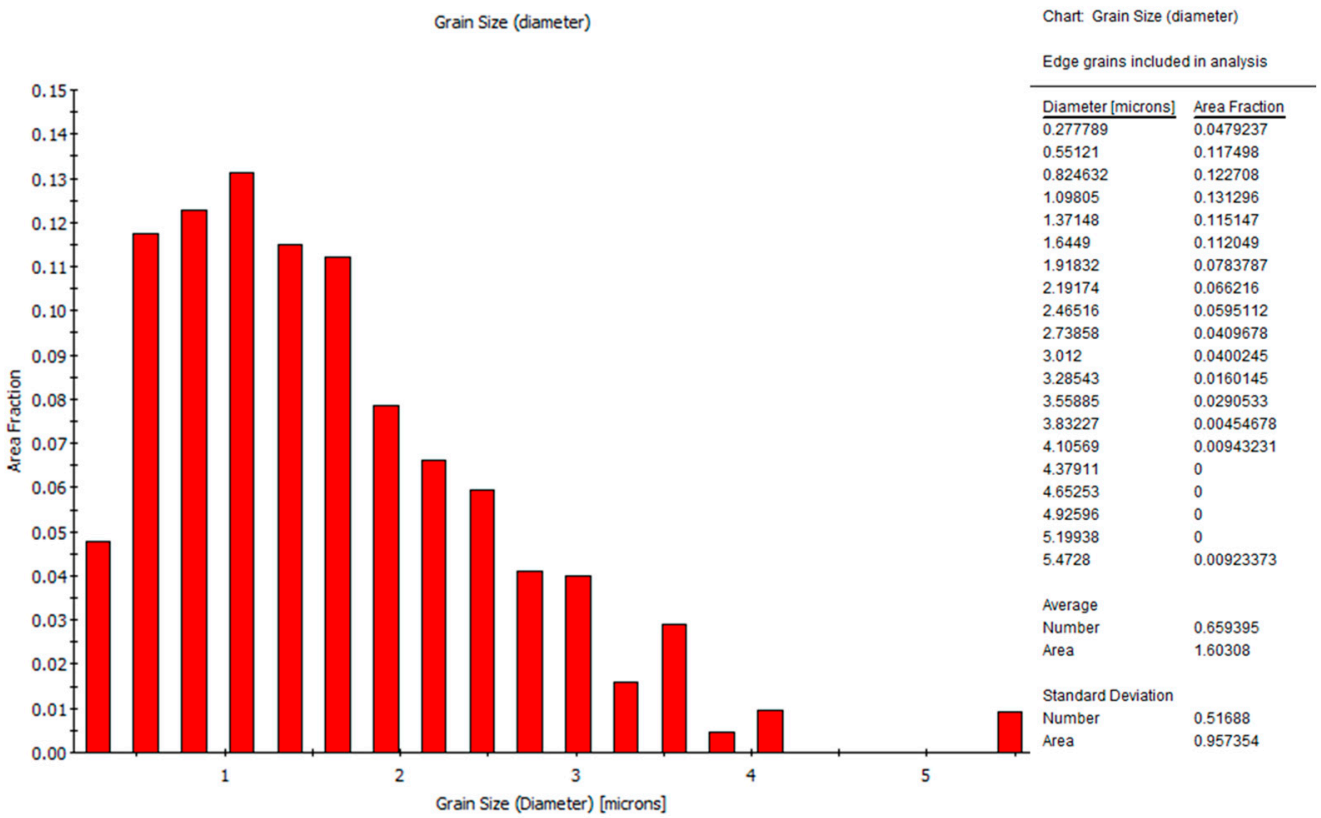


Figure 5. QP1180 base metal grain size distribution histogram.

The SEM images of the welded pair of 1.2 mm QP980 steel with 1.5 mm QP1180 steel are shown in Figure 6. As can be understood from the cross-section macro view of the weld seam, defect-free joining is established through the thickness of the pairs (Figure 6a). The SEM examinations indicated that the microstructure of the FZ completely consisted of lath M grains (Figure 6b). The microstructure of the supercritical HAZ of QP980 steel also consisted of the M phase with an equiaxed grain morphology (Figure 6c). In the medium critical HAZ, the laser fusion-induced temperature rise may have reached below the AC3 temperature, leading to the formation of both M and F grains in the microstructure (Figure 6d). The microstructural features of the BM are mostly alike in the sub-critical HAZ of the QP980 side (Figure 6e). The microstructural features of the QP1180 side reflected similar characteristics to those of the 1.2 mm thick QP980 side. Namely, a microstructure consisting of TM in the supercritical HAZ (Figure 6f), a microstructure consisting of M and F in the inner parts of the medium critical of the HAZ (Figure 6g), and a microstructure consisting of TM in the outer sub-critical parts of the HAZ (Figure 6h) were evident. However, a finer microstructure seemed to form at the fusion-induced microstructural evolution regions of the 1.5 mm thick QP1180 steel.

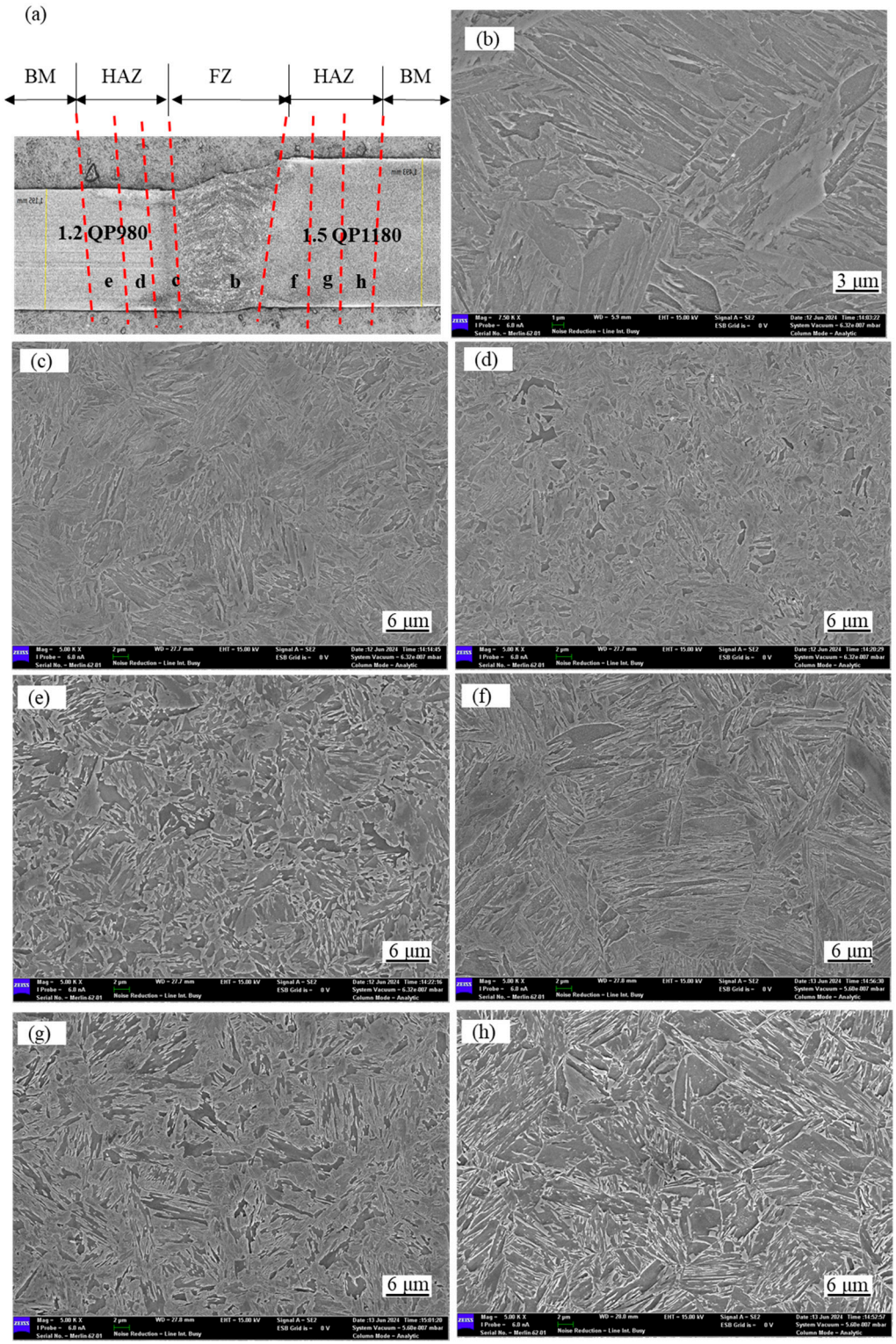


Figure 6. SEM micrographs of the microstructure of 1.2 mm QP980–1.5 mm QP1180 laser-welded joint: (**a**) a macro-overview of the welding area; (**b**) FZ (completely martensite); (**c**–**e**) the HAZ of QP980; (**f**–**h**) the HAZ of QP1180.

3.1.2. Microstructure of Laser-Welded 1.2 mm QP980 and 1.5 mm QP1180 Steels

Crystallographic orientation distribution maps showing the changes in the microstructural properties of the BM, HAZ, and FZ after the laser welding of dissimilar 1.2 mm QP980–1.5 mm QP1180 steels are shown in Figure 7. It is understood from the microstructure of the FZ that, after the melting and resolidification pairs, the as-received microstruc-

tures transformed into an FZ microstructure that fully consisted of lath-type M phase. From Figure 7b, it is understood that the RA phase with an FCC structure is almost non-existent in the microstructure of the FZ (Figure 7b). It is important to note that the sub-boundaries with very low crystallographic orientation variations exist within martensite grains separated with HAGBs. These sub-boundaries are oriented nearly parallel to the crystallographic orientation of the M grains (Figure 7a,b). This led to the existence of HAGBs with a volume fraction of 38.2% in the FZ microstructure that mainly consisted of the lath M phase (Figure 7c). The microstructure of the QP980 steel side mostly reflects similar microstructural features to the as-received steel at the HAZ (Figure 7d–f). The microstructure can be characterized by the existence of fine M and RA, determined as 6.4% (Figure 7e), which is lower than that of the as-received counterpart (Figure 2b). When the characteristics of the grain boundaries are examined, it is understood that the volume fraction of the HAGBs is determined as 80% (Figure 7f). This value is lower than that of the volume fraction of the HAGBs in the microstructure of the as-received counterpart (88%). Simultaneous decreases in the HAGB and RA volume fraction may occur due to the increase in the volume fraction of the M phase in the HAZ microstructure of the QP980 steel. The microstructure of the HAZ region on the QP1180 side consisted of F, M, and RA phase grains. The volume fraction of RA was determined as 9% without a significant change compared to that of the as-received steel (Figure 7h). Boundaries in the structure consist of HAGBs with a volume fraction of 75% comparable to that of the as-received counterpart (Figure 7i). When the average grain sizes (Figure 8a) measured from the FZ and HAZ regions are evaluated, it is important to note that the FZ consists of coarser grains with an average size of about 0.65 μm. The average grain size of the microstructures formed in the HAZs of QP980 and QP1180 steels was determined to be about 0.56 μm (Figure 8b,c). From these values, it is understood that a grain coarsening that significantly changes the average grain size of the HAZ region does not occur during welding. This can be considered a good indicator of the compatibility of the QP980 and QP1180 steels with the laser welding process.

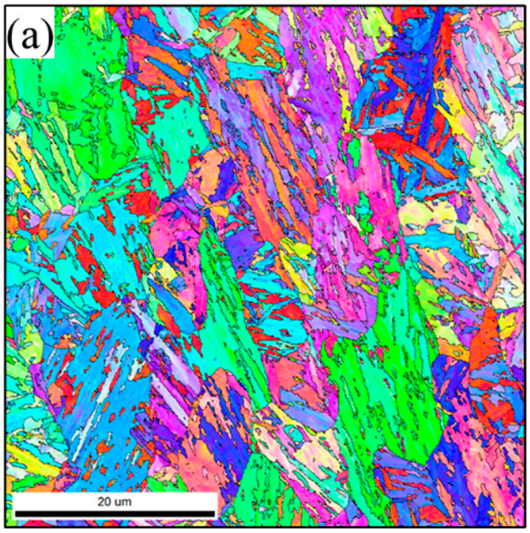


Figure 7. *Cont.*

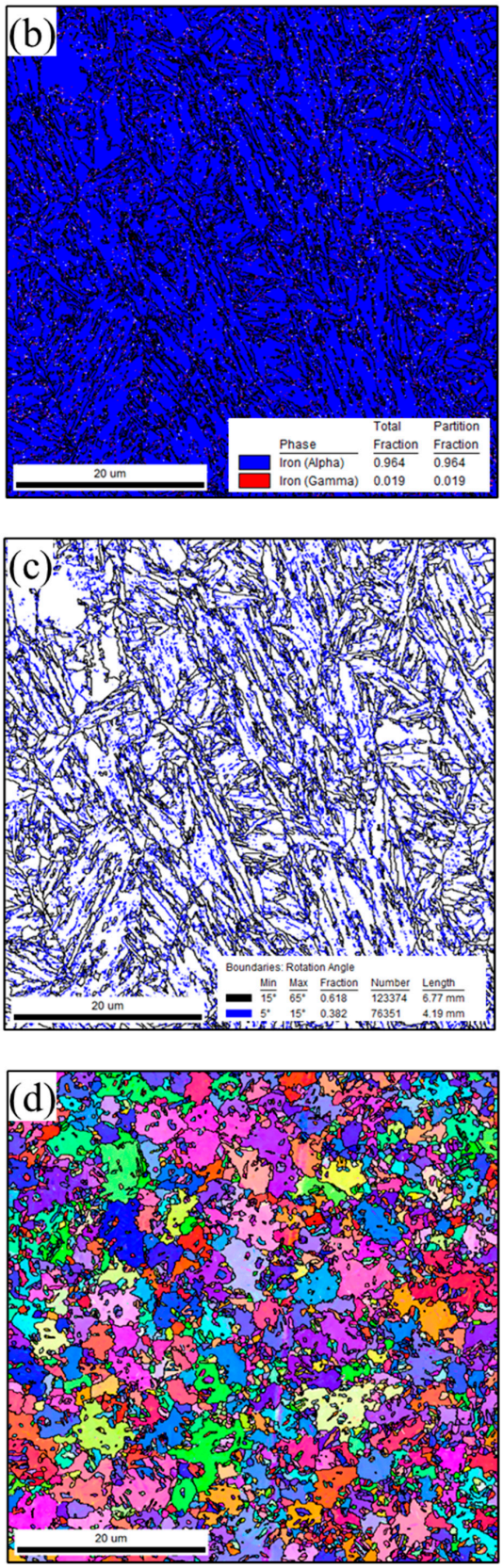


Figure 7. *Cont*.

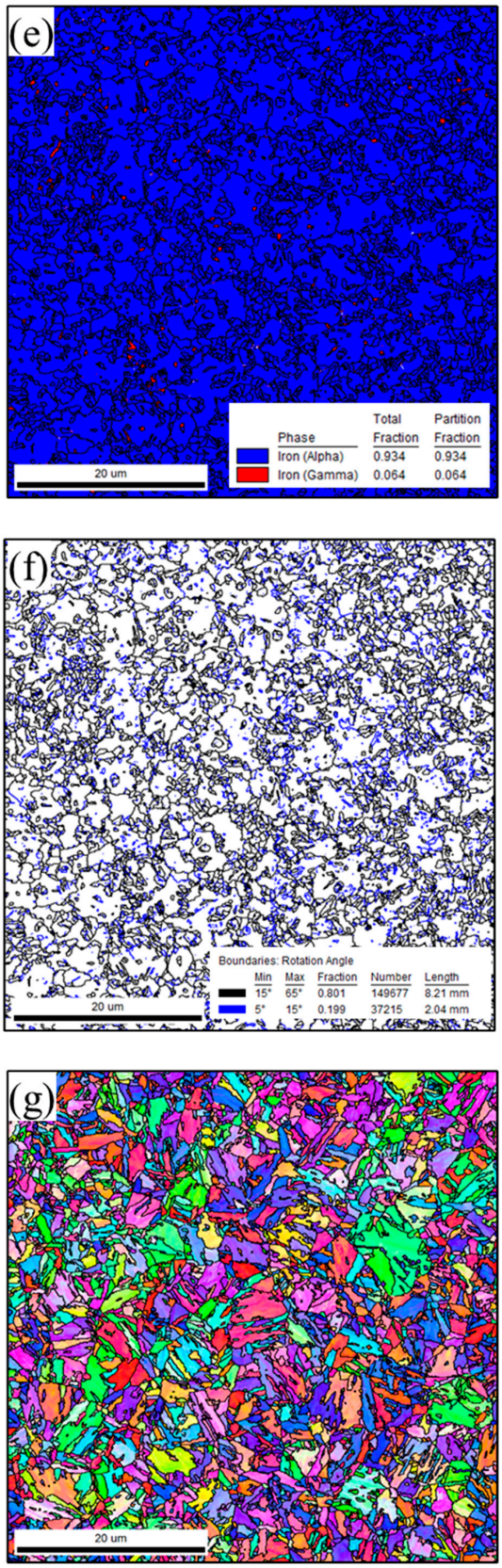


Figure 7. *Cont*.

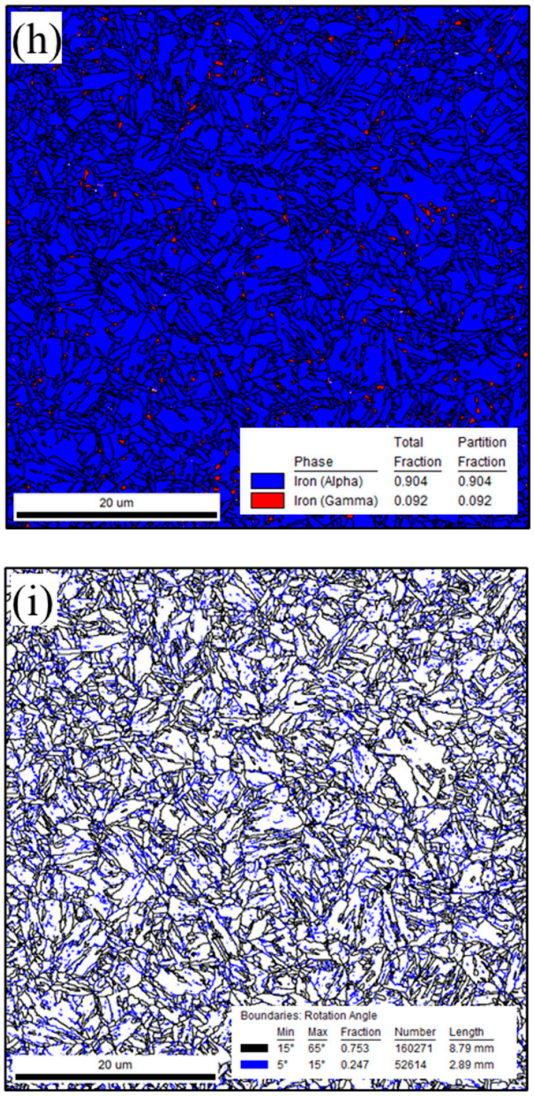


Figure 7. Internal structure shapes of 1.2 mm QP980 and 1.5 mm QP1180 steels after laser welding, showing orientation maps, phase distributions, and grain boundary characteristics, respectively: (**a**–**c**) HAZ region of laser-welded steels; (**d**–**f**) HAZ region of QP980 steel; (**g**–**i**) HAZ region of QP1180 steel.

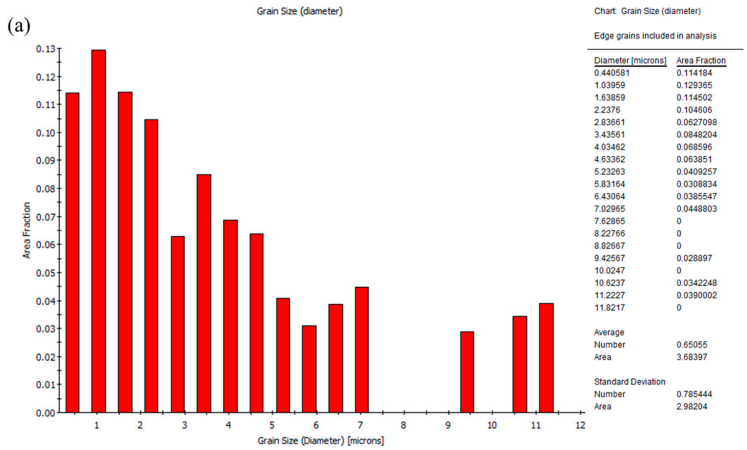


Figure 8. *Cont*.

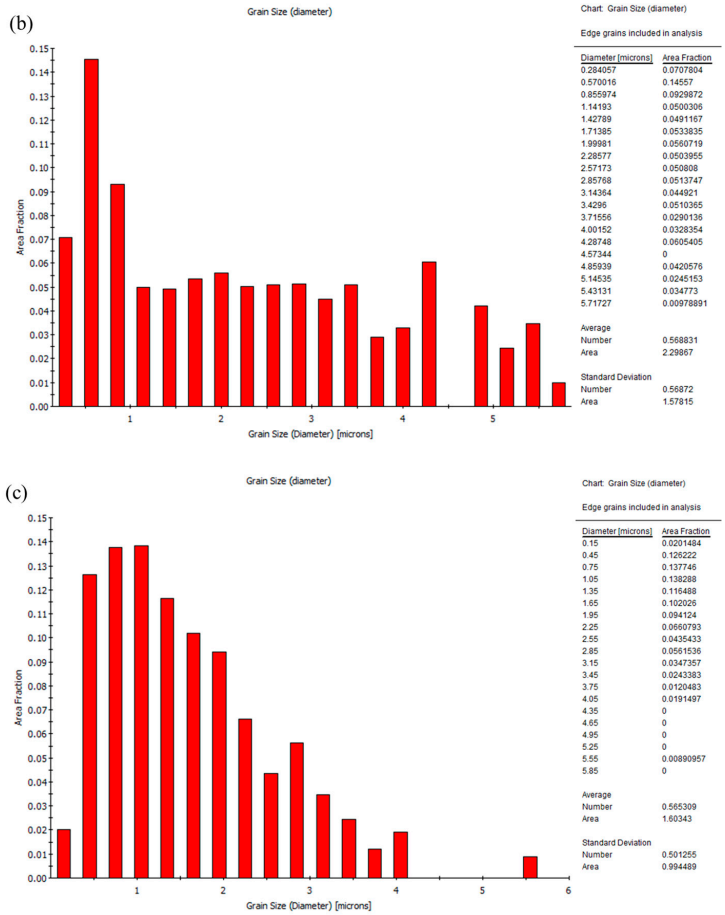


Figure 8. Histograms of 1.2 mm QP980 and 1.5 mm QP1180 steels in HAZ region after laser welding: (**a**) FZ; (**b**) HAZ region of QP9800 steel; (**c**) HAZ region of QP1180 steel.

3.2. Mechanical Characterization

3.2.1. Microhardness Measurement

Figure 9 presents the variation in the microhardness values through the measurement path extending over the HAZ, FZ, and BM. The hardness values of the BMs of QP980 and QP1180 steels were measured as 380 Hv and 400 Hv, respectively. The microhardness of FZ took a considerably higher hardness value of about 510 Hv. These results are in accordance with previous publications. Guo et al. showed that the QP980-QP980 dissimilar steel joints were fabricated by fiber laser welding in their study. The FZ of laser-welded QP980 steel composed of a fully martensitic structure exhibited high hardness (493 Hv). The sub-critical HAZ contained partially tempered martensite with a hardness drop (21 Hv) [30]. In their study, Li et al. showed that QP980-QP980 dissimilar steel joints were fabricated by fiber laser welding. The FZ was composed of lath martensite with a high microhardness (499 HV). Martensite tempering was found at the sub-critical heat-affected zone, resulting in a slight decrease in microhardness (~37 HV drop) [30]. In their study, Zahrani et al. fabricated the 1.2 mm QP980-QP980 dissimilar steel joints by fiber laser welding. The results reveal that the FZ and upper-critical HAZ comprised full martensite with a high microhardness. The HAZ contained at least a 48 HV microhardness drop because of martensite tempering [22]. Moreover, the hardness values slightly changed, though the HAZ of both QP980 and QP1180 sides showed a plateau profile. The hardness value decreased sharply to the BM hardness levels by the end of the HAZ. Consequently, the hardness profile of the laser-welded pair did not show any soft region due to the RA value being 8.4% (Figures 2b and 4b). The formation of this profile is attributed to both changes in the chemical composition of the FZ and phase transformation during the cooling

stage of the welded pair. The chemical composition of the fusion zone is assumed to be changed due to the simultaneous melting of the pairs of dissimilar QP980-QP1180 steels. Due to the no filler materials are used for laser welding final chemical composition of the fusion zone may occur because of the basic law of mixture [31]. Based on the basic rule of mixture, the chemical composition of the FZ reaches an alternative state after the pairs are melted and blended. In the current case, the chemical compositions of the QP980 and QP1180 steels are similar. Consequently, the final chemical composition and critical cooling rate for the M transformation of the FZ are expected to be identical to those of the pairs. Since laser welding applies a local and concentrated source of energy, the temperature of the HAZs seems to increase to levels above AC3, leading to the transformation of the microstructure into austenite. In the cooling stage, the transformation of the austenite to M may be responsible for the formation of a large plateau in the hardness profile of the pair. M phase-dominated microstructures of the FZ and HAZ support this idea (Figure 6).

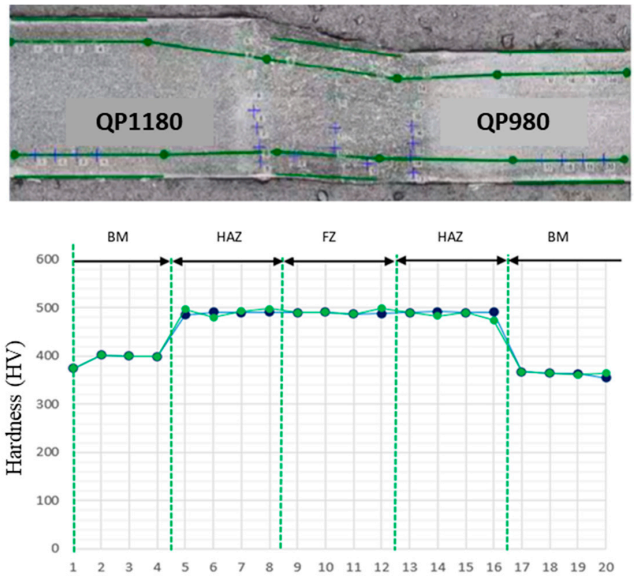


Figure 9. Microhardness measurements of 1.5 mm QP1180 and 1.2 mm QP980 laser-welded steels.

3.2.2. Tensile Tests

Engineering strain vs. engineering stress curves and images of the BMs and laser-welded steels are presented in Figures 10 and 11, respectively. BMs are reflected in the expected deformation behaviors of QP980 and QP1180. The mechanical properties of the BMs and laser-welded steels are shown in Table 2. The yield strength of the BM of the 1.2 mm QP980 steel was about 801.3 MPa and reached an ultimate tensile strength of about 1050.7 MPa with the aid of uniform elongation of about %14.7. After tensile strength was applied, ductile fracture occurred at the elongation of about 17.2%. The 1.5 mm QP1180 steel reflected higher yield strength and tensile strength values of 1042.4 MPa and 1180 MPa, respectively. The steel showed uniform elongation and elongation to failure values of about 9.7% and 12.4%, respectively. Tensile deformation was primarily concentrated in the softened zone and was small in the fusion zone. It is important to note that QP steels exhibited a good combination of strength and ductility with the aid of the well-engineered microstructure consisting of the well-balanced ductile F and hard M phases. Also, RA in the microstructure well supported strain hardenability through the transformation-induced plasticity effect (TRIP effect). By the synergetic effect of these microstructural constituents, both QP980 and QP1180 steels reflected a strain hardening dominated plastic deformation that promotes requirements of both manufacturing and load-bearing performance.

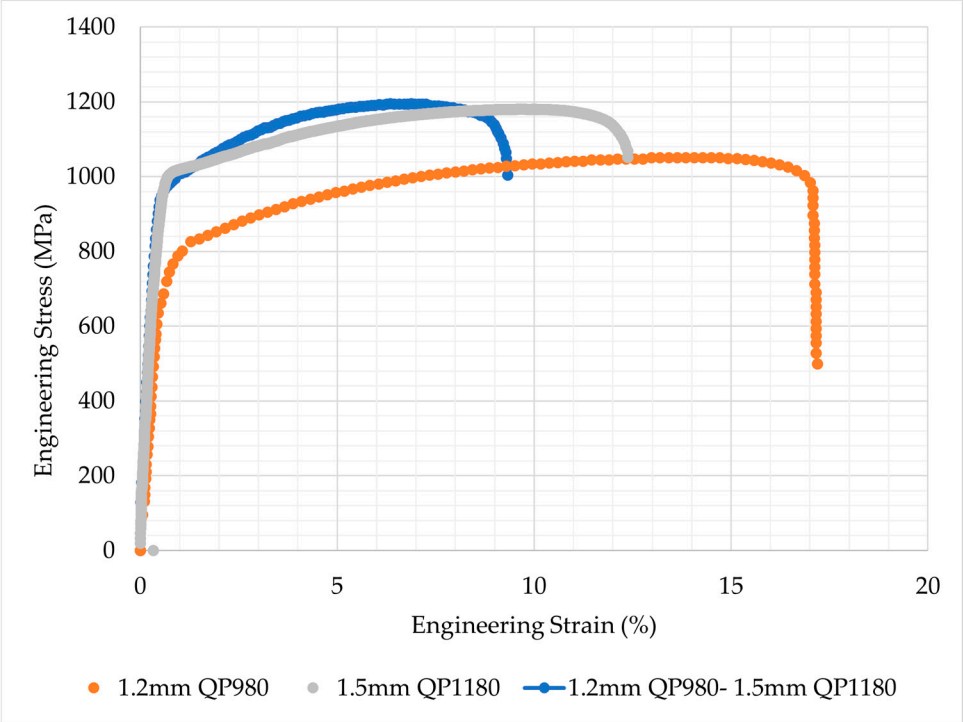


Figure 10. Tensile test results of BMs and 1.2 mm QP980–1.5 mm QP1180 laser-welded steels.

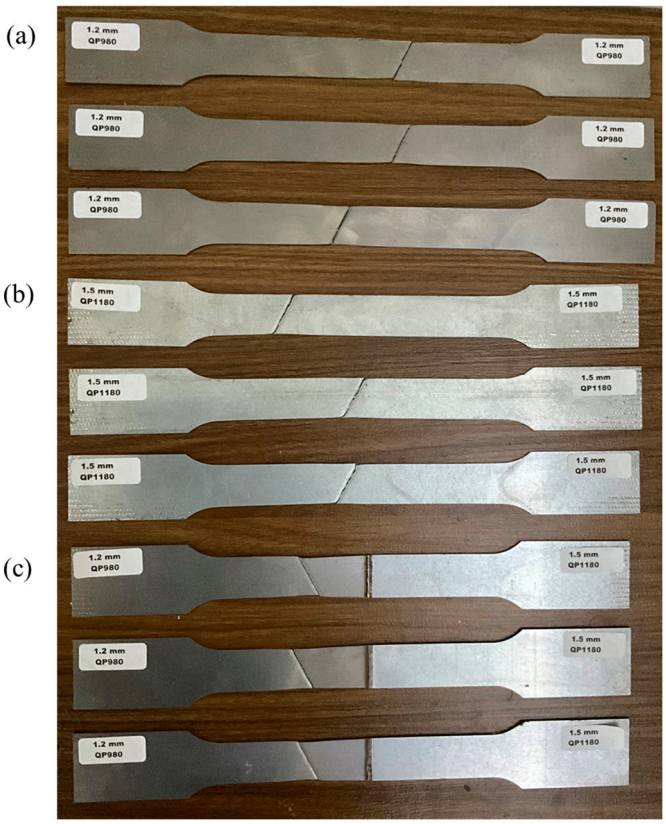


Figure 11. Images of tensile strength samples after test: (**a**) 1.2 mm QP980; (**b**) 1.5 mm QP1180; (**c**) laser-welded 1.2 mm QP980; and 1.5 mm QP1180 steels.

Table 2. Mechanical properties of BMs and 1.2 mm QP980–1.5 mm QP1180 laser-welded steels.

Sample	Yield Strength (MPa)			Tensile Strength (MPa)			Uniform Elongation (%)			Elongation to Failure (%)			Fracture Location
1.2 QP980	801.3	±	2.3	1050.7	±	2.3	14.7	±	0.2	17.2	±	0.5	BM
1.5 QP1180	1042.4	±	25.8	1180.0	±	5.5	9.7	±	0.4	12.4	±	0.5	BM
1.2 QP980–1.5 QP1180	816.6	±	45.8	1194.2	±	21.9	6.9	±	2.6	9.3	±	1.7	QP980-BM

Mechanical testing of the laser-welded pair showed deformation behavior similar to that of the QP980 steel. As can be understood from Figure 10 and Table 2, the laser-welded pair yielded a stress level of about 816.6 MPa and reached an ultimate tensile strength of about 1194.2 MPa with the aid of the uniform elongation of about 6.9%, and it finally failed after an elongation of 9.3%. However, the ductility of the pair is lower than that of the QP980 steel. These mechanical properties and the deformation behavior can be explained by considering the microstructural evolution and hardness profile of the welding region. The formation of the M phase-dominated microstructure at the FZ and HAZ of welded steels led to the formation of a high-strength region (Figure 7). By the end of the HAZ, the hardness values sharply decreased to the BM hardness values at the border of HAZ-BM. This made the low-strength partner of the joint dictate the mechanical properties of the joint. However, the sharp transition in strength levels may have also caused a variation in deformation behavior, leading to deformation localization. Localized deformation may have caused an earlier onset of necking in the gauge length of the QP980 steel. Consequently, uniform elongation and elongation to failure of the QP980 steel may be measured to have lower values compared to those of the steel in the as-received condition [31–33]. In their study, Zahrani et al. fabricated 1.2 mm QP980-QP980 dissimilar steel joints by fiber laser welding. The yield and tensile strengths were 841 and 1270 MPa, respectively, which represented reductions of 5.5% and 0.78% compared to the base material properties [22]. These mechanical properties simply indicate that the pair showed a strength performance comparable to that of the QP980 steel. However, the ductility of the pair is lower than that of the QP980 steel. These mechanical properties and the deformation behavior can be explained by considering the microstructural evolution and hardness profile of the welding region. The formation of the M phase dominated the microstructure at the FZ and HAZ of welded steels, which led to the formation of a high-strength region (Figure 6). By the end of the HAZ, the hardness values sharply decreased to the BM hardness values at the border of HAZ-BM. This made the low-strength partner of the joint dictate the mechanical properties of the joint. However, the sharp transition in strength levels may have also caused a variation in the deformation behavior, leading to deformation localization. The localized deformation may have caused an earlier onset of necking in the gauge length of the QP980 steel. Consequently, the uniform elongation and elongation to failure of the QP980 steel may be measured to have lower values compared to those of the steel in the as-received condition. These results are in accordance with previous publications. Tensile deformation was primarily concentrated in the softened zone and was small in the FZ [22].

3.2.3. Erichsen Tests

A standard Erichsen cupping test can reflect the biaxial stretch formability of the welded joints. The test specimens after the Erichsen Cupping tests were applied to the BMs and welded samples are shown in Figure 12. When this figure is examined, it is seen that the deformation behavior of the hardening effect seen in the tensile experiments caused the samples to turn into domes of different heights. Sample damage was caused by crescent-shaped cracks in the areas where the contact of the deformed sample with the spherical punch was interrupted. This damage is a characteristic behavior observed in most metals suitable for plastic deformation [34]. With this feature, it was evaluated that

the general deformation behavior of the samples in the as-received state was compatible with the studies in the literature [30,35]. The spherical punch force (F)–punch displacement (X) curves recorded during the Erichsen tests of the BMs and welded steels are given in Figure 13. The highest punch force obtained from the curves and the corresponding displacement values are given in Table 3. It is seen that the F-X curve characteristics obtained from the Erichsen tests applied to the BMs and welded pair are similar to each other. Table 3 indicates that 1.2 mm QP980 steel reached a dome height of 9.99 mm under a load of 60.81 kN, and QP1180 steel reached a dome height of 8.62 mm under a load of 71.79 kN. The welded pair, on the other hand, reached a peak punch load of 42.55 kN with a punch displacement of 6.98 mm. It is important to note that both the largest punch forces and the Erichsen indexes exhibited by the welded pair are lower than the values exhibited by the as-received steels. Figure 14 shows the appearance of laser-welded steels after the Erichsen test. According to this figure, it is important to note that the welded samples were damaged along a line that cut the weld seam. This may be considered a good indicator of the absence of a soft zone in the weld seam. Moreover, this fracture mode explains the lower values of the punch force and Erichsen index of the welded pair than those of the as-received counterparts. The deformation mode of the samples that underwent the Erichsen test includes the biaxial tensile straining of the sample under a semi-spherical punch. During this deformation, the weld seam and HAZ act as high-strength resistors to the punch displacement and transformation of the plain sample into a dome due to the M microstructure. It is known that the ductility values of M structures are limited compared to other phases in the Fe-C system. This causes the weld seam to fracture after a limited punch displacement due to the brittle fracture tendency and limited strain hardenability. It is well known that martensite formation is a diffusion-less transformation that generates volume change and, consequently, great internal stresses. Internal stresses cause the plastic deformation of the martensite phase grains to require higher energy than that required for fracture. Consequently, martensite grains show a higher yield strength but early onset of fracture after yielding. This makes the martensite phase show a high cracking tendency.



(**a**) (**b**) (**c**)

Figure 12. Images of samples after undergoing Erichsen cupping test: (**a**) 1.2 mm QP980; (**b**) 1.5 mm QP1180; (**c**) laser-welded 1.2 mm QP980; and 1.5 mm QP1180 steels.

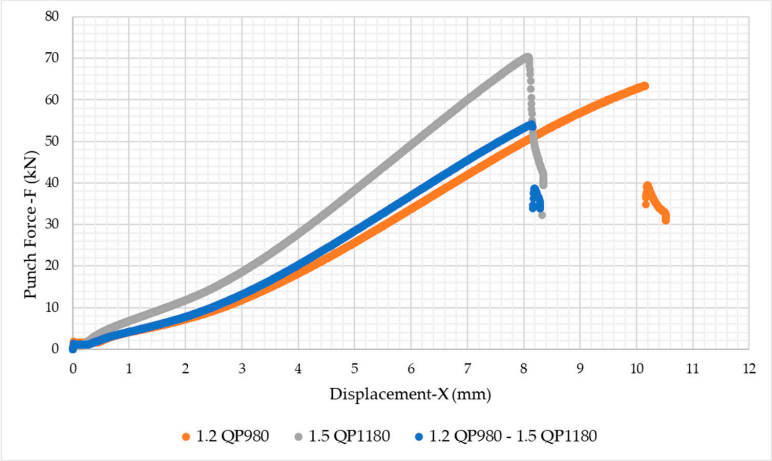


Figure 13. Graph of punch force (F)–punch displacement (X) curves of BMs and 1.2 mm QP980–1.5 mm QP1180 welded steels.

Table 3. Punch force (F)–displacement (X) curves and fracture location of BMs and 1.2 mm QP980–1.5 mm QP1180 laser-welded steel sheets.

Sample	Punch Force (F) (kN)			Erichsen Index (mm)			Fracture Location
1.2QP980	60.81	±	1.9	9.99	±	0.4	BM
1.5QP1180	71.79	±	1.9	8.62	±	0.2	BM
1.2 QP980-1.5 QP1180	42.55	±	10.2	6.98	±	1.0	Weld seam

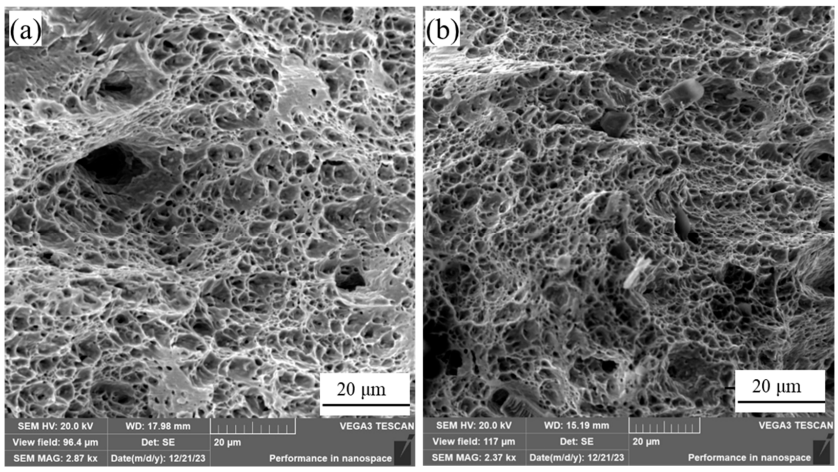


Figure 14. Fracture surface images of tensile-tested 1.2 mm QP980–1.5 mm QP1180 welded steel samples: (**a**) shows flat brittle surfaces and dimples; (**b**) shows dimples.

3.3. Fractography

SEM photographs showing the fracture surfaces of the welded steel samples after the tensile test are presented in Figure 14a,b to reveal the effect of laser welding on the fracture behavior of the joints. The 1.2 mm QP980–1.5 mm QP1180 joint was fractured with ductile characteristics with the formation of dimples, where micro-cracks were formed, propagated, and coalesced until the fracture of the necking region occurred. These results are in accordance with previous publications. Guo et al. investigated the dissimilar QP980–QP980 steel joints fabricated by fiber laser welding, and all joints failed at the BM, showing a typical ductile fracture [30]. Since the fracture surface presents shallow dimples and flat brittle fracture features, it can be said that the fracture has both ductile and brittle characteristics. The source of the brittle characteristics on the fracture surface may be related to a considerably higher volume fraction of the hard M phase.

SEM photographs showing the fracture surfaces of the BMs after the Erichsen test are shown in Figure 15a–d. Samples of QP980 and QP1180 underwent fracture after significant thinning (Figure 15a–c). Such thinning may be considered an indicator of high ductility because of the excellent strain hardenability. As a result of this deformation behavior, the fracture surface of the QP980 steel can be characterized by the existence of deep dimples (Figure 15b). The fracture surface of the 1.5 mm QP1180 steel mainly consisted of shallow dimples (Figure 15d). The difference between the as-received QP980 and QP1180 steels is attributed to the volume fraction of the M. It can be said that with the increase in the volume ratio of M, the continuity of the F phase decreases remarkably. This may also decrease the contribution of strain hardening due to the narrower dislocation accumulation sites, leading to limited dislocation interactions, the early onset of deformation localization, and fracture. The fracture surface of the Erichsen-tested welded pair is shown in Figure 15e,f. The fracture surface of the welded seam can be characterized by the formation of the large separation sites along the weld seam without a strong sign of plastic deformation behavior like thinning. This fracture behavior may have occurred due to the increased cracking tendency of the fusion zone and/or weld seam due to the transformation of the microstructure into the martensite phase.

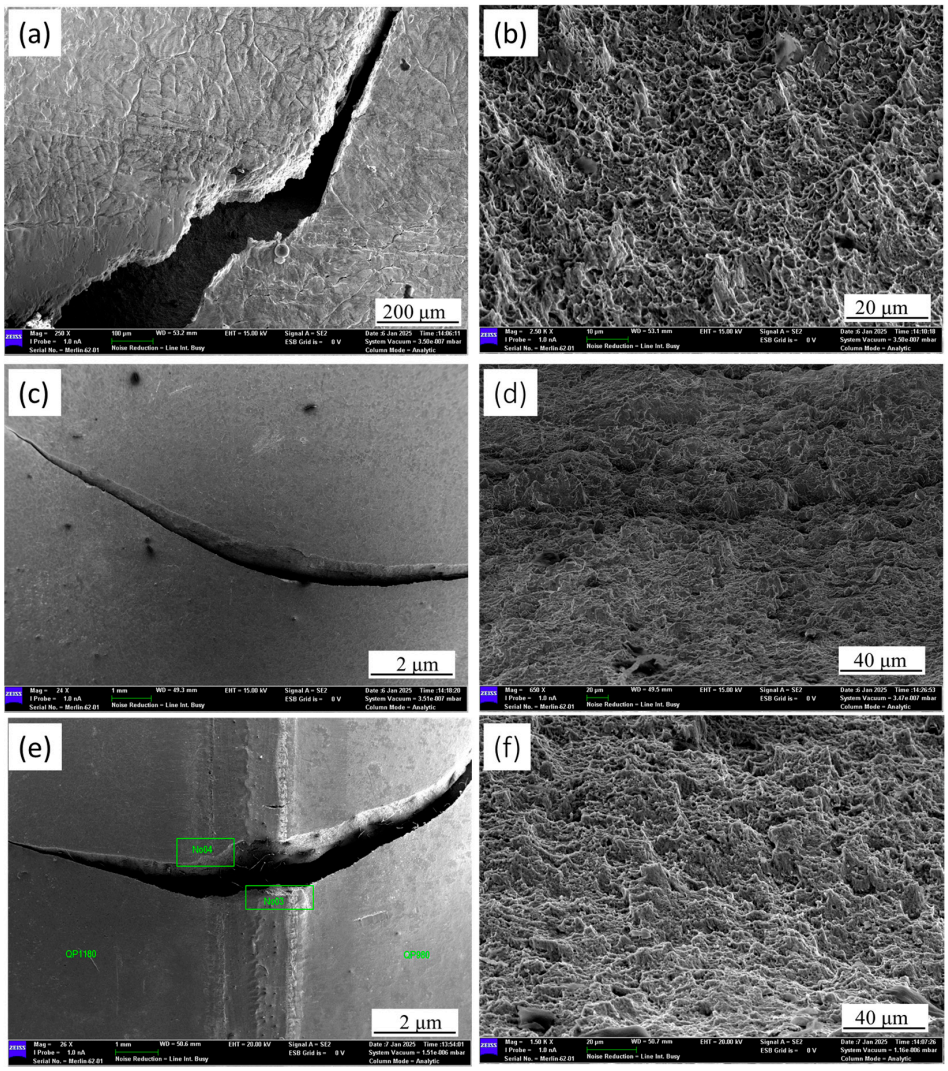


Figure 15. SEM photographs of the fracture surfaces of BMs and welded steels after the Erichsen cupping test: (**a**,**b**) QP980 BM; (**c**,**d**) QP1180 BM; and (**e**,**f**) 1.2 mm QP980–1.5 mm QP1180 laser-welded joint.

4. Conclusions

In this study, the microstructural evolution, mechanical properties, and deformation behavior of the laser-welded joints between third-generation 1.2 mm QP980 and 1.5 mm QP1180 steel sheets were investigated. The following conclusions were drawn based on the experimental results obtained from the microstructural examinations (SEM and EBSD), hardness, tension, and Erichsen cupping tests:

(a) Laser welding 1.2 mm QP980 and 1.5 mm QP1180 steels resulted in a microstructure that consisted of a lath M phase in FZ. The microstructure of QP980 and QP1180 steels consists of the M phase at the supercritical HAZ and is transformed into a microstructure that consists of RA, F, and M in the sub-critical HAZ.

(b) The hardness of the BMs of QP980 and QP1180 were measured as 380 Hv and 400 Hv, respectively. The microhardness of the FZ of the joint was measured as 510 Hv. This value is considerably higher than those of both BMs. The hardness value of the HAZ reflected a limited variation through the HAZ of both the QP980 and QP1180 sides. The HAZ hardness values decreased sharply to the BM hardness levels by the end of the sub-critical HAZ.

(c) The yield and tensile strengths of the welded steels were measured as 816.6 MPa and 1194.2 MPa, respectively. The uniform elongation and elongation at break values of these steels were determined as 6.9% and 9.3%, respectively.

(d) The laser-welded pair showed an Erichsen index of 6.98 mm, which is 70% of that of the 1.2 QP980 steel. This value is acceptable for industrial applications of QP steel. The lower Erichsen index of the pair is mainly attributed to the full M microstructure of the weld seam, leading to the early onset of fracture at the biaxial tensile loading of the Erichsen test.

Dissimilar joining of high-strength materials is a continuously growing research interest in the automotive industry. It offers considerable flexibility in designing lightweight and tailored multi-material parts made of different grades of steel or multiple thicknesses for specific purposes. For instance, the multi-thickness assembly was widely used in laser tailor-welded blanks to make A and B pillar and door rings in actual production. Multi-thickness assembly can decrease the weight and the cost of parts. However, the mechanical properties and microstructures of dissimilar AHSS joints are always quite different from those of the base materials. The results of the current study simply indicate that dissimilar laser welding of QP1180 and QP980 steels can be achieved without a considerable strength loss and an acceptable level of formability. These findings may provide designers in the automotive industry with an idea about the mechanical performance of welded joints and where the laser welding seam will be applied according to the performance expectations of the part, including where the part will deform and fail if the laser weld seam is applied.

Within the scope of this study, the focus is on the formation of third-generation high-strength steel sheets joined by the fiber laser welding method. It is understood that steels combined with laser welding offer a reasonable design opportunity in terms of formability. As a result, it seems possible to obtain superior automobile parts from the forming of tailor-welded blanks of QP steels joined by laser welding.

Author Contributions: Conceptualization, H.Ç. and O.S.; methodology, H.Ç. and O.S.; validation, H.Ç. and O.S.; investigation, H.Ç.; writing—original draft preparation, H.Ç.; writing—review and editing, H.Ç. and O.S.; visualization, H.Ç.; supervision, O.S. All authors have read and agreed to the published version of the manuscript.

Funding: This research received no external funding.

Data Availability Statement: The raw data supporting the conclusions of this article will be made available by the authors on request.

Acknowledgments: The authors would like to acknowledge that this paper is submitted for partial fulfillment of the requirements for a PhD degree at Bursa Technical University. The authors would like to thank Baosteel (Baoshan Iron & Steel Co., Ltd.) for their support during this investigation.

Conflicts of Interest: Author Hafize Çelik was employed by the company Tofaş Türk Otomobil Fabrikası A.Ş. The remaining authors declare that the research was conducted in the absence of any commercial or financial relationships that could be construed as a potential conflict of interest.

Abbreviations

The following abbreviations are used in this manuscript:

AHSS	Advanced High-Strength Steel
BIW	Body in White
BM	Base Metal
EBSD	Electron Backscatter Diffraction
EL	Elongation
F	Ferrite
FZ	Fused Zone
HAGB	High Angle Grain Boundaries
HAZ	Heat-Affected Zone
Hv	Microhardness Vickers
LME	Liquid Metal Embrittlement
M	Martensite
QP	Quenching and Portioning
RA	Retained Austenite
TM	Tempered Martensite
TRIP	Transformation-Induced Plasticity
UTS	Ultimate Tensile Strength
YS	Yield Strength

References

1. Billur, E.; Çetin, B.; Gürleyik, M. New Generation Advanced High Strength Steels: Developments, Trends and Constraints. *Int. J. Sci. Technol. Res.* **2016**, *2*, 50–62.
2. European Commission and CRU. European Commission and CRU. Available online: https://commission.europa.eu/index_en (accessed on 1 June 2021).
3. Stellantis. Stellantis: Official Global Website. Available online: https://www.stellantis.com/en/company/dare-forward-2030/care (accessed on 18 July 2024).
4. Grajcar, A.; Morawiec, M.; Różański, M.; Stano, S. Twin-spot laser welding of advanced high-strength multiphase microstructure steel. *Opt. Laser Technol.* **2017**, *92*, 52–61. [CrossRef]
5. Fonstein, N. *Dual-Phase Steels in Automotive Steels*; Woodhead Publishing: Sawston, UK, 2017; pp. 169–216. [CrossRef]
6. Butuc, M.C.; Vincze, G.; Santos, R.; Pereira, A.; Santos, A.D.; Amaral, R.L.; Barlat, F. Formability of third generation advanced high strength steel: Experimental and theoretical approach. *Int. J. Mech. Sci.* **2024**, *281*, 109559. [CrossRef]
7. Bao Steel Company. Baowu Open Innovation. Available online: http://rd.baosteel.com/zypt/en/ability/see/abilityDetailsBSSF5/1/318362afb3924a479c3bb4407ce48f6a (accessed on 1 March 2024).
8. World Auto Steel. The Latest Global Formability Diagram. Available online: https://www.worldautosteel.org/ahss-insights-blog-the-new-global-formability-diagram (accessed on 3 March 2022).
9. Demir, S.; Doruk, E. New generation steels for light weight vehicle safety related applications. *Mater. Test.* **2024**, *66*, 992–998. [CrossRef]
10. Bai, S.B.; Chen, Y.A.; Sheng, J.; Li, D.Z.; Lu, H.H.; Bai, P.K.; Huang, Z.Q.; Li, J.Y.; Zhao, C. A comprehensive overview of high strength and toughness steels for automobile based on QP process. *J. Mater. Res. Technol.* **2023**, *27*, 2216–2236. [CrossRef]
11. Shome, M.; Tumuluru, M. *Introduction to Welding and Joining of Advanced High-Strength Steels (AHSS) in Welding and Joining of Advanced High-Strength Steels (AHSS)*; Woodhead Publishing: Sawston, UK, 2015; pp. 1–8, ISBN 9780857098580.

12. Aydin, H.; Tutar, M.; Davut, K.; Bayram, A. Effect of welding current on microstructure and mechanical properties of 15% deformed TWIP steel joined with electrical resistance spot welding. *J. Fac. Eng. Archit. Gazi Univ.* **2021**, *35*, 803–817. [CrossRef]
13. Tuncel, O.; Aydın, H.; Çetin, Ş. Nd: Yag lazer kaynağı ile birleştirilen DP600 çeliğinde darbe süresinin mikroyapı ve mekanik özelliklerine etkisi. In Proceedings of the 9th International Automotive Technologies Congress, OTEKON, Bursa, Türkiye, 7–8 May 2018; Available online: https://www.otekon.org/dokuman/books/9thOtekonBook.pdf (accessed on 15 June 2018).
14. Farabi, N.; Chen, D.L.; Zhou, Y. Microstructure and mechanical properties of laser welded dissimilar DP600/DP980 dual-phase steel joints. *J. Alloys Compd.* **2011**, *509*, 982–989. [CrossRef]
15. Wang, Z.W.; Liu, M.; Zhang, H.; Xie, G.M.; Xue, P.; Wu, L.H.; Zhang, Z.; Ni, D.R.; Xiao, B.L.; Ma, Z.Y. Welding behavior of an ultrahigh-strength quenching and partitioning steel by fusion and solid-state welding methods. *J. Mater. Res. Technol.* **2022**, *17*, 1289–1301. [CrossRef]
16. Ertem, R.U. Investigation of The Effect of The Laser Welding Parameters Change on Welding Seam for Stainless Steel. *Sigma J. Eng. Nat. Sci.* **2013**, *31*, 583–593. Available online: https://dergipark.org.tr/en/pub/sigma/issue/65813/1026759 (accessed on 1 December 2013).
17. Turan, M.K.; Yuce, C.; Karpat, F. Numerical and experimental investigation of the effect of heat input on weld bead geometry and stresses in laser welding. *Mater. Test.* **2024**, *66*, 1463–1474. [CrossRef]
18. Zhao, L.L.; Lu, Y.; Xue, R.J.; Zhang, Q.; Gao, Y.Z.; Nian, B.G.; Ma, C. Microstructure Characterization and Mechanical Properties of Laser Welded Super High Strength QP980 Automotive Steel. *Solid State Phenom.* **2023**, *354*, 99–116. [CrossRef]
19. Xue, J.; Guo, W.; Zhang, Y.; Xia, M.; Jia, Q.; Chi, J.; Shi, J.; Wu, Y.; Zhang, H. Local microstructure and mechanical characteristics of HAZ and tensile behavior of laser welded QP980 joints. *Mater. Sci. Eng.* **2022**, *854*, 143862. [CrossRef]
20. Guo, W.; Wan, Z.; Peng, P.; Jia, Q.; Zou, G.; Peng, Y. Microstructure and mechanical properties of fiber laser welded QP980 steel. *J. Mater. Process. Technol.* **2018**, *256*, 229–238. [CrossRef]
21. Zhang, C.; Tian, J.; Yang, S.; Mu, S. Effect of water-cooling assistance on fatigue behavior of laser welded QP980 steel. *J. Mater. Res. Technol.* **2024**, *28*, 2060–2070. [CrossRef]
22. Zahrani, M.M.; Ranjbarnodeh, E.; Ketabchi, M.; Ghassemali, E. Microstructure evolution and mechanical properties of laser-welded joints of 1.2 GPa-class quenching and partitioning steel. *Opt. Laser Technol.* **2024**, *170*, 110257. [CrossRef]
23. Fang, K.; Yang, J.G.; Song, K.J.; Liu, X.S.; Fang, H.Y. Acceleration of regeneration treatment for nanostructured bainitic steel by rotary impacting trailed welding. *J. Mater. Process. Technol.* **2014**, *214*, 2935–2940. [CrossRef]
24. Farabi, N.; Chen, D.L.; Zhou, Y. Tensile properties, and work hardening behavior of laser-welded dual-phase steel joints. *J. Mater. Eng. Perform.* **2012**, *21*, 222–230. [CrossRef]
25. Xue, J.; Peng, P.; Guo, W.; Xia, M.; Tan, C.; Wan, Z.; Zhang, H.; Li, Y. HAZ Characterization and Mechanical Properties of QP980-DP980 Laser Welded Joints. *Chin. J. Mech. Eng. Ji Xie Gong Cheng Xue Bao* **2021**, *34*, 80. [CrossRef]
26. Huang, J.; Li, S.; Zhong, H.; Xiao, S.; Li, D. Microstructure, Mechanical Properties, and Corrosion Behavior of Laser-Welded Dissimilar Joints Between DP980 and QP980 Steel. *Steel Res. Int.* **2022**, *93*, 2100541. [CrossRef]
27. Guo, Y.; Wu, Y.; Zhang, W.; Xu, M.; Li, L.; Wu, Z. Investigation on microstructure and properties of dissimilar joint between TRIP800 and QP980 fabricated by laser welding. *Sci. Technol. Weld. Join.* **2021**, *26*, 161–172. [CrossRef]
28. Jia, Q.; Guo, W.; Wan, Z.; Peng, Y.; Zou, G.; Tian, Z.; Zhou, Y.N. Microstructure, and mechanical properties of laser welded dissimilar joints between QP, and boron alloyed martensitic steels. *J. Mater. Process. Technol.* **2018**, *259*, 58–67. [CrossRef]
29. Zhao, H.; Huang, R.; Sun, Y.; Tan, C.; Wu, L.; Chen, B.; Song, X.; Li, G. Microstructure, and mechanical properties of fiber laser welded QP980/press-hardened 22MnB5 steel joint. *J. Mater. Res. Technol.* **2020**, *9*, 10079–10090. [CrossRef]
30. Li, W.; Ma, L.; Peng, P.; Jia, Q.; Wan, Z.; Zhu, Y.; Guo, W. Microstructural evolution and deformation behavior of fiber laser welded QP980 steel joint. *Mater. Sci. Eng. A* **2018**, *717*, 124–133. [CrossRef]
31. Dak, G.; Pandey, C. A critical review on dissimilar welds joints between martensitic and austenitic steel for power plant application. *J. Manuf. Process.* **2020**, *58*, 377–406. [CrossRef]
32. Xue, B.; Li, Y.; Yi, W.; Shi, S.; Dai, Y.; Liu, C.; Ren, M.; He, C. Biaxial Very High Cycle Fatigue Testing and Failure Mechanism of Welded Joints in Structural Steel Q345. *Crystals* **2024**, *14*, 850. [CrossRef]
33. Výrostková, A.; Homolová, V.; Pecha, J.; Svoboda, M. Phase evolution in P92 and E911 weld metals during ageing. *Mater. Sci. Eng. A* **2008**, *480*, 289–298. [CrossRef]
34. Saray, O.; Purcek, G.; Karaman, I.; Maier, H.J. Formability of ultrafine-grained interstitial-free steels. *Metall. Mater. Trans. A* **2013**, *44*, 4194–4206. [CrossRef]
35. Santos, R.O.; Pereira, A.B.; Butuc, M.C.; Vincze, G.; Festas, A.J.; Moreira, L.P. Development of a device compatible with universal testing machine to perform hole expansion and Erichsen cupping tests. *Machines* **2019**, *8*, 2. [CrossRef]

Disclaimer/Publisher's Note: The statements, opinions and data contained in all publications are solely those of the individual author(s) and contributor(s) and not of MDPI and/or the editor(s). MDPI and/or the editor(s) disclaim responsibility for any injury to people or property resulting from any ideas, methods, instructions or products referred to in the content.